Microscopic dynamics of superfluid ^{4}He: A comprehensive study by inelastic neutron scattering

K. Beauvois,[1,2] J. Dawidowski,[3] B. Fåk,[1] H. Godfrin,[2] E. Krotscheck,[4,5] J. Ollivier,[1] and A. Sultan[2]

[1]*Institut Laue-Langevin, CS 20156, 38042 Grenoble Cedex 9, France*

[2]*Université Grenoble Alpes, CNRS, Grenoble INP, Institut Néel, 38000 Grenoble, France*

[3]*Comisión Nacional de Energía Atómica and CONICET, Centro Atómico Bariloche, (8400) San Carlos de Bariloche, Río Negro, Argentina*

[4]*Department of Physics, State University of New York at Buffalo, Buffalo, New York 14260, USA*

[5]*Institute for Theoretical Physics, Johannes Kepler University, A 4040 Linz, Austria*

(Received 23 February 2018; revised manuscript received 4 May 2018; published 30 May 2018)

The dynamic structure factor of superfluid ^{4}He has been investigated at very low temperatures by inelastic neutron scattering. The measurements combine different incoming energies resulting in an unprecedentedly large dynamic range with excellent energy resolution, covering wave vectors Q up to 5 Å^{-1} and energies ω up to 15 meV. A detailed description of the dynamics of superfluid ^{4}He is obtained from saturated vapor pressure up to solidification. The single-excitation spectrum is substantially modified at high pressures, as the maxon energy exceeds the roton-roton decay threshold. A highly structured multiexcitation spectrum is observed at low energies, where clear thresholds and branches have been identified. Strong phonon emission branches are observed when the phonon or roton group velocities exceed the sound velocity. The spectrum is found to display strong multiexcitations whenever the single excitations face disintegration following Pitaevskii's type a or b criteria. At intermediate energies, an interesting pattern in the dynamic structure factor is observed in the vicinity of the recoil energy. All these features, which evolve significantly with pressure, are in very good agreement with the dynamic many-body calculations, even at the highest densities, where the correlations are strongest.

DOI: 10.1103/PhysRevB.97.184520

I. INTRODUCTION

Understanding the dynamics of correlated bosons is a subject of general interest in several fields of physics. Bose-Einstein condensation and superfluidity [1,2], first found in ^{4}He, are fundamental phenomena that imprint remarkable signatures on the dynamics of these systems. Experimentally, superfluid ^{4}He is the simplest example of strongly correlated bosons. The interaction potential is particularly well known, and substantial effort has been devoted to develop a coherent theoretical framework that can describe and explain the extraordinary properties of this quantum fluid [1–11]. The theoretical methods can be generalized to other many-body problems, including, for instance, up-to-date approaches of the complex case of correlated fermions [12–16].

The prediction by Landau [3] of the phonon-roton excitation spectrum of superfluid ^{4}He and its direct observation in the dynamic structure factor $S(Q,\omega)$ using neutron scattering techniques [4,17] are cornerstones of modern physics, at the origin of the present microscopic descriptions of matter [5,18,19]. The dynamics of superfluid ^{4}He at very low temperatures, in the vicinity of the ground state, is dominated by the "phonon-maxon-roton" excitation branch. The corresponding excitations, extremely sharp, correspond essentially to poles of the dynamic density-density response function. They are referred to as "single excitations" in the neutron scattering literature, and as "quasiparticles" in theoretical works. An effective description of the dynamics of such systems can be obtained in terms of these modes, allowing, for instance, a very accurate statistical evaluation of the low-temperature thermodynamic properties [4,20].

Sharp excitations are absent above twice the roton energy [4,17,21], and the dynamics at intermediate energies is described in terms of broad excitations, named "multiexcitations" for reasons described below. Multiexcitations still have a significant statistical weight in the dynamic structure factor [4,17,22–30]. Their spectrum is known to display some structure since the early measurements of Svensson, Martel, Sears, and Woods [23]. More recent investigations [24–29] showed that some features could be ascribed to multiexcitations. These were related to pairs of high density-of-states roton (R) and maxon (M) modes (denoted hereafter as $2R$, $2M$, and MR). The broad ridges observed in $S(Q,\omega)$ at saturated vapor pressure (SVP) (see Fig. 1 of Ref. [24]) and at 20 bars (see Fig. 1 of Ref. [29]) were consistent with the calculated energies of the main combinations ($2R$, $2M$, and MR).

A much finer structure in the dynamic response was observed in our recent work at zero pressure [30], including sharp thresholds, narrow branches, and a new two-phonon decay process, the "ghost phonon." Explaining this rich dynamic response, observed from the continuum limit to subatomic distances, constitutes a challenge and an opportunity for microscopic theories. Finally, at high energies, the dynamic structure factor gradually approaches a quasi-free-particle behavior [22] described by the impulse approximation [4,17,31].

Even though helium is one of the most intensively investigated physical substances, measurements covering a large kinetic range are scarce. The canonical results by Cowley and Woods [22], Dietrich *et al.* [32], or Svensson *et al.* [23] have a low resolution by modern standards, while later measurements specialize in specific ranges [27–29,33,34]. Our extensive high-resolution measurements, presented in Fig. 1, provide

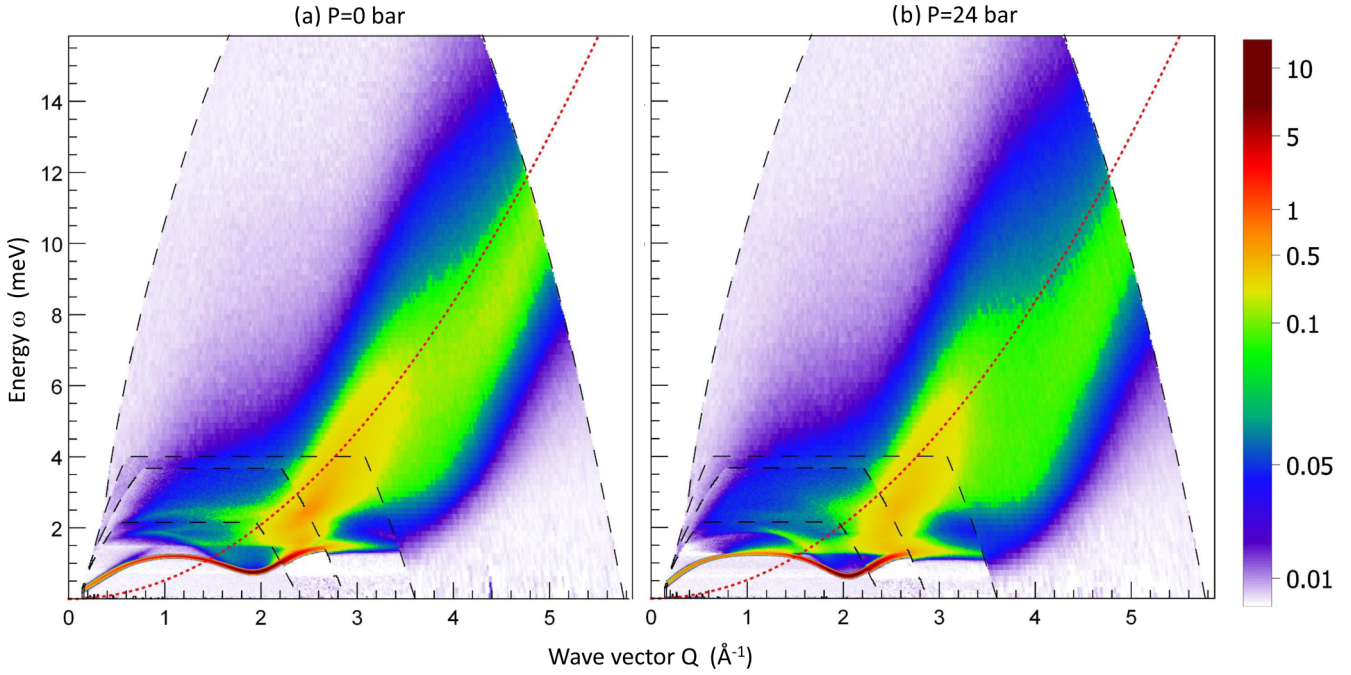

FIG. 1. $S(Q,\omega)$ of superfluid ^{4}He as a function of wave vector and energy transfer, measured at $T \leqslant 100$ mK at (a) saturated vapor pressure ($P \approx 0$) and (b) near solidification ($P = 24$ bars). The plots combine data measured at different incident neutron energies ($E_i = 3.55$, 5.1, 8.00, and 20.45 meV) for an optimum energy resolution; the dashed black lines represent the limits of the corresponding kinetic ranges. The dotted red line is the free ^{4}He atom recoil energy $E_r = \frac{\hbar^2 Q^2}{2M}$. The color-coded intensity scale is in units of meV^{-1}.

a detailed and complete map of the dynamics of superfluid ^{4}He. In addition to its aesthetic merits, the picture shows new features that are the object of this paper.

Helium is highly compressible. Since the atomic correlations depend on the density, it is interesting to investigate the pressure dependence of the density excitations. Much of the earlier work has been focused on the effect of pressure on the single-excitation response, in order to determine, for example, the Landau parameters characterizing the dispersion curve. The multiexcitation spectrum has also been found experimentally [27–29,32–35] and theoretically [4,7,9,36] to be strongly modified by the pressure. It was therefore desirable to extend our recent high-sensitivity measurements [30] to finite pressures, and more particularly near solidification, where theory [9] predicted radical changes in the dynamics.

In this paper, we present a detailed investigation of the effect of pressure on the dynamics of superfluid ^{4}He. We cover a large energy and wave-vector range while preserving the resolution needed to observe the fine structure of the spectra. High-resolution maps of the dynamic structure factor $S(Q,\omega)$ have been obtained at SVP and at $P = 24$ bars, close to solidification, as shown in Fig. 1. Additional measurements have been made in a smaller dynamic range at the intermediate pressures 5 and 10 bars. We finally compare our data to microscopic calculations of $S(Q,\omega)$ within the dynamic many-body theory [9] performed at the densities corresponding to the experimental pressure conditions.

II. EXPERIMENTAL DETAILS

The measurements were performed on the IN5 time-of-flight spectrometer at the high-flux reactor of Institut Laue Langevin. Our previous work [30] at low temperatures and saturated vapor pressure used cold neutrons of energy $E_i = 3.55$ meV. In the present work, we combine data taken using four different incident neutron energies, $E_i = 3.55, 5.11, 8.00$, and 20.45 meV, for which the energy resolution [full width at half-maximum (FWHM)] at elastic energy transfer was 0.070, 0.12, 0.23 and 0.92 meV, respectively. This allowed us to obtain a complete map of the dynamic structure factor at the most relevant pressures, i.e., saturated vapor pressure (SVP) and near solidification ($P = 24$ bars). We also investigated a few intermediate pressures using $E_i = 3.55$ meV.

The cylindrical sample cell was made out of aluminum 5083, with 1 mm wall thickness and 15 mm inner diameter [30]. Cadmium disks of 0.5 mm thickness were placed inside the cell every centimeter to reduce multiple scattering. The cell was thermally connected to the mixing chamber of a very-low-temperature dilution refrigerator using massive OFHC copper pieces. Heat exchangers made out of sintered silver powder were used to provide a good thermal contact with the helium sample. Care was taken to thermally anchor the filling capillary at several places along the dilution unit in order to reduce heat leaks to the cell. The measurements were all performed at very low temperatures, well below 100 mK, i.e., essentially at zero temperature for the properties under investigation.

High-purity (99.999%) helium gas was condensed in the cell at low temperatures, using a gas-handling system including a "dipstick" cold trap operated in a helium storage dewar. The dipstick was used to condense the gas and to pressurize the helium sample. The pressure in the system was measured with a precision of 6 mbars with a 0–60 bars Digiquartz gauge located at the top of the cryostat. The corresponding precision for the pressures inside the cell is 20 mbars after applying helium

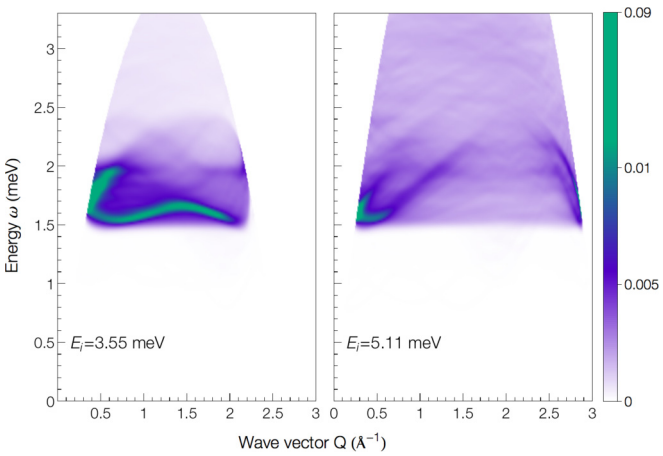

FIG. 2. Monte Carlo calculation of the contribution of double-scattering within the helium to $S(Q,\omega)$. Results are shown for two incident neutron energies, $E_i = 3.55$ and 5.11 meV. The color-coded intensity scale is in units of meV^{-1}.

hydrostatic head corrections. The actual pressures in the cell for the nominal 0, 5, 10, and 24 bars are essentially 0 (SVP at 100 mK), 5.01(2), 10.01(2), and 24.08(2) bars.

III. DATA REDUCTION

Standard time-of-flight data reduction [37] was used to obtain the dynamic structure factor $S(Q,\omega)$ from the raw data. The contribution of the cell scattering was subtracted, as well as that of double-scattering events of the type "inelastic helium scattering plus elastic scattering from the cell." This type of double scattering is essentially independent of wave vector.

The contribution of the multiple scattering within the helium was corrected using Monte Carlo simulations [38]. Due to the small diameter of our sample cell and the presence of several cadmium plates, multiple-scattering corrections are small (the ratio of double-scattered to single-scattered neutrons is on the order of 1% [30]), but they may be comparable to the multiexcitation signal. It is therefore essential to verify that multiple scattering is not contaminating the spectra in the energy and wave-vector regions of interest, and to perform the corrections when necessary, in particular at low Q.

Since multiple scattering depends on the incident neutron energy, as shown in Fig. 2, while multiexcitations do not, Monte Carlo calculations can be used to select the most appropriate incident neutron energy for the experiments, and also to experimentally distinguish multiexcitations from multiple scattering.

The only input needed by the Monte Carlo simulations [38] in the present case is the initially measured scattering function $S(Q,\omega)$ after corrections for multiple-scattering processes involving the cell, and the coherent scattering cross section of ^{4}He, $\sigma_c = 1.34$ barns. We first calculate the total scattering cross section [38,39] $\sigma_s(E_i)$:

$$\sigma_s(E_i) = \frac{N\sigma_c}{2k_i^2}\int Q\,dQ\int S(Q,\omega)d\omega, \qquad (1)$$

where N is the number of scatterers and k_i is the incident neutron wave vector.

We find $\sigma_s(E_i = 3.55\ \text{meV}) = 0.64$ barns, about one-half of the coherent scattering cross section σ_{coh}. The multiple scattering fraction is 0.8% for $E_i = 3.55$ meV, increasing slightly with pressure from 0.79% at SVP to 1.06% at 24 bars. This agrees well with calculations using the semianalytical method developed by Sears [40], which give values increasing from 0.93% to 1.09% for the same pressures. Multiple scattering can be seen in the experimental spectra at low wave vectors, thus providing a way to check the Monte Carlo calculations used to eliminate this effect. This is a crucial step in the data analysis, needed to ensure that all the features we report in $S(Q,\omega)$ do indeed correspond to multiexcitations.

The calculated contribution due to multiple scattering within the helium has been subtracted from the spectra measured using incident neutron energies $E_i = 3.55$ and 5.11 meV. This was found to be unnecessary for $E_i = 8.00$ and 20.45 meV, because multiple scattering processes are negligible in the corresponding regions of the "combined" spectra of Fig. 1.

An overall scale factor was applied to $S(Q,\omega)$ at SVP, so that the weight of the single excitation $Z(Q)$ agrees with that of Cowley and Woods [22] near the roton, i.e., $Z(Q = 2\ \text{Å}^{-1}) = 0.93$ at SVP. At higher pressures, the same scaling factor was used, but corrected for the density ratio $\rho(P)/\rho(P = 0)$.

IV. EXPERIMENTAL RESULTS

A. Spectra at SVP and $P = 24$ bars in a large dynamic range

Our comprehensive results on the dynamic structure factor $S(Q,\omega)$ at SVP and $P = 24$ bars are shown in Fig. 1. These maps were obtained by combining the four different neutron energies. Higher energies make a larger dynamic range accessible, but the instrumental energy resolution deteriorates rapidly (see Sec. II). Since the corresponding dynamic ranges have a substantial overlap, we can select the most appropriate data set in terms of resolution, neutron counts, or cleanest background for each region of the Q-ω plane. The $S(Q,\omega)$ maps are built in the following way: first, the spectrum measured at $E_i = 3.55$ meV is represented; outside its useful kinetic range, the data at $E_i = 5.11$ meV are added, then the data at $E_i = 8.00$ meV, and finally the data at $E_i = 20.45$ meV.

The constant wave-vector scans presented in Fig. 3, obtained as particular "cuts" of Fig. 1, provide a complementary perspective on the data. The phonon-roton single-excitation mode is very narrow at the scale of Figs. 1 and 3, and the observed width is essentially a measure of the experimental energy resolution (with the remarkable exception of the maxon at high pressures, which is discussed in the next section). The influence of a finite energy resolution is clearly seen in Fig. 1 as a width discontinuity in the Pitaevskii plateau [4,21], between ranges corresponding to different incident neutron energies. It is important to note, however, that the experimental broadening effects are negligible in all the *multiexcitation* region investigated in the present work (except at the end of the Pitaevskii plateau).

Merging data measured with different resolutions has been successfully achieved, judging from the remarkable continuity in intensity between the different regions represented in Fig. 1. This is essentially due to the fact that the sharpest multiexcitations are found in the low-energy

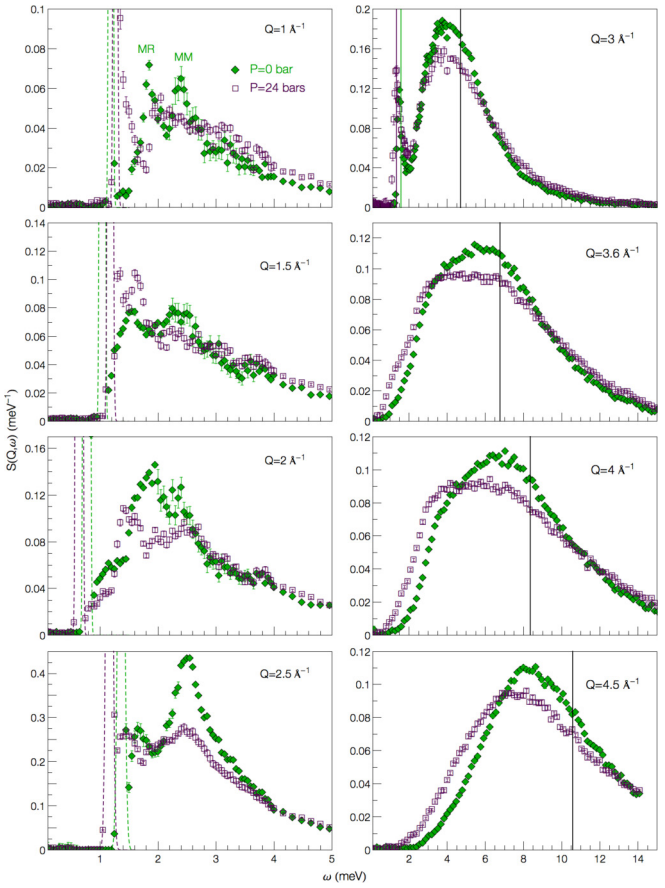

FIG. 3. Dynamic structure factor $S(Q,\omega)$ combining data at four incident neutron energies: spectra for different wave vectors Q at SVP (green diamonds) and $P = 24$ bars (purple squares). The dashed lines are Gaussian fits of the resolution-limited phonon-roton peaks (off scale). The black lines represent the helium recoil energy. At $Q = 3$ Å^{-1}, the purple and green lines represent the two-roton energy $2\Delta_R$ at SVP and $P = 24$ bars, respectively. At $Q = 1$ Å^{-1}, MR and MM are the energy positions at SVP of the maxon-roton and maxon-maxon multiexcitations, respectively.

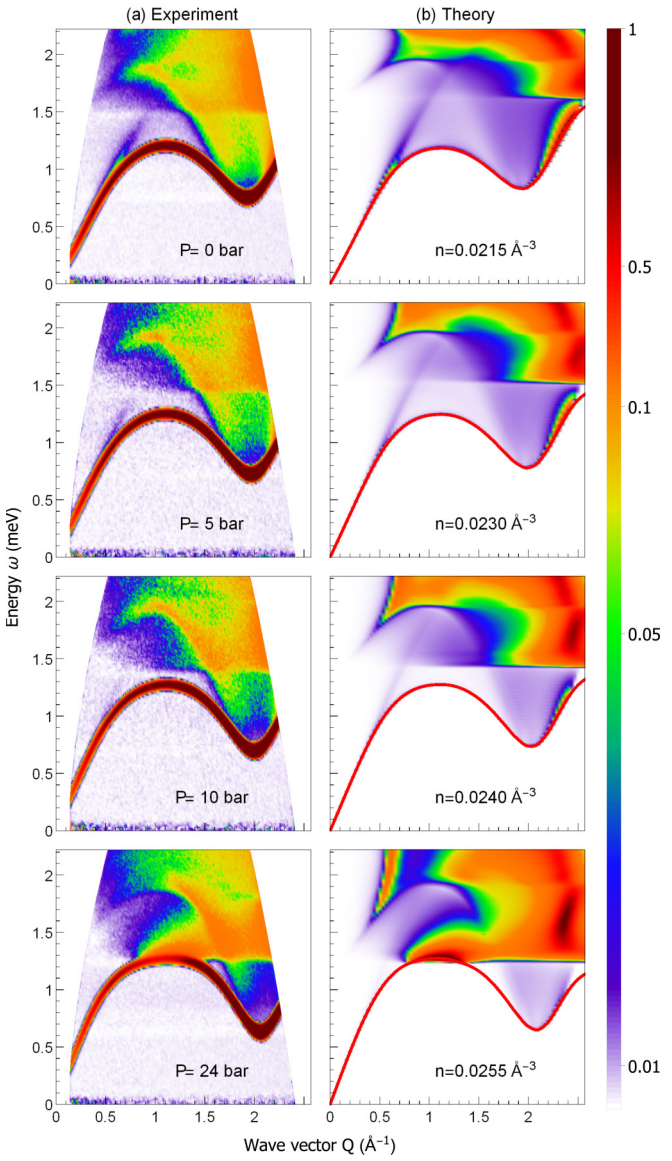

FIG. 4. (a) $S(Q,\omega)$ of superfluid ^{4}He measured as a function of wave vector and energy transfer, at $P = 0$, 5, 10 and 24 bars and temperature $T \leqslant 100$ mK. The incident neutron energy is $E_i = 3.55$ meV. (b) Dynamic many-body theory calculation of $S(Q,\omega)$ at corresponding densities ($n = 0.0215$, 0.0230, 0.0240, and 0.0255 Å^{-3}; see the text). Note that the main features of the experimental data are well reproduced. The color-coded intensity scale is in units of meV^{-1}. The intensity is cut off at 1 meV^{-1} in order to emphasize the multiexcitations region. The apparent width of the phonon-roton excitations in the experimental plot is due to an energy resolution of 0.07 meV, while the calculated phonon-roton dispersion curve has been highlighted by a thick red line.

and low-wave-vector sector, adequately covered by our high-resolution data at $E_i = 3.55$ and 5.11 meV. Conversely, the spectra in the quasi-free-particle region, at high energies and wave vectors, are intrinsically broad and adequately covered by our data at 8.00 and 20.45 meV, in spite of their lower resolution. Using optimized incident neutron energies reveals the complete evolution of the system, characterized by several multiexcitation branches merging progressively at high wave vectors to form a broad but rather intense feature. Intensity in this region was observed in early studies [4,17], but the data were either strongly truncated [24,25,29] or measured with low resolution [22]. This feature finally becomes, after a strong oscillation, a less intense branch progressively approaching the free-particle parabolic dispersion.

B. High-resolution spectra as a function of pressure

We present in this section the spectra obtained using an incident neutron energy of $E_i = 3.55$ meV for wave vectors up to $Q = 2.5$ Å^{-1} and energies up to $\omega = 2.22$ meV. The results are shown in Fig. 4(a), where we represent our earlier data [30] at SVP, the present data at 5 and 10 bars, and the data at $P = 24$ bars discussed in the previous section. One can readily note that both the single-excitation and multiexcitation components of the dynamic structure factor are modified by the pressure.

Our results for the single-excitation dispersion measured at several pressures, shown in Fig. 5(a), are in excellent agreement with previous works [4,17,24,25,28,32,34,41,42]. The roton

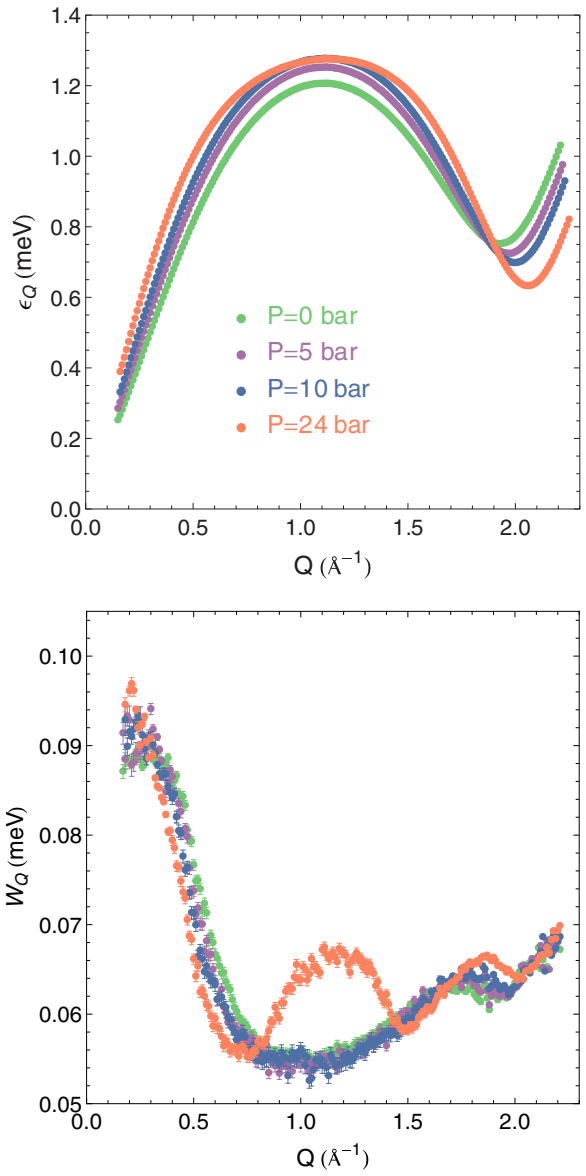

FIG. 5. (a) Dispersion relation $\epsilon_Q(Q)$ of the single excitations measured at 0, 5, 10, and 24 bars. Note the flattening of the curve at the maxon at high pressures. (b) The wave-vector dependence of the measured width (FWHM) of the single-excitation peaks. The measured width reflects the shape of the experimental resolution ellipsoid cut by the dispersion relation curve at different angles. At 24 bars, however, a physical broadening of the maxon is clearly observed.

parameters at each pressure have been obtained from fits of the single-excitation dispersion relation $\epsilon_Q(Q)$ to the expression

$$\epsilon_Q = \Delta_R + \frac{\hbar^2}{2m\mu_R}(Q - Q_R)^2 + b(Q - Q_R)^3 + c(Q - Q_R)^4, \quad (2)$$

where Δ_R is the roton energy gap, Q_R is the wave vector at the roton minimum, and μ_R is the roton effective mass; b and c are additional adjustable parameters. Fits were made over a total wave-vector range ΔQ up to 0.47 Å^{-1}. Due to the large number of individual detectors and the high neutron rate of IN5,

TABLE I. Roton energy gap Δ_R, wave vector of the roton minimum Q_R, and roton effective mass μ_R; values in parentheses are one-standard-deviation errors from least-squares fits described in the text.

P (bars)	Δ_R (meV)	Q_R (Å^{-1})	μ_R
0	0.7416(10)	1.9260(2)	0.1240(4)
5.01(2)	0.7143(10)	1.9655(2)	0.1096(4)
10.01(2)	0.6885(10)	1.9963(2)	0.1000(4)
24.08(2)	0.6254(10)	2.0579(2)	0.0879(4)

the statistical uncertainty of the fits is very good (see Table I). The roton mass determined in our work is lower than the one obtained by Andersen *et al.* [24,25] using a parabolic fit of the roton minimum, but it agrees well with earlier measurements [41] where the parabolic fit was limited to a very narrow wave-vector range.

A similar analysis can be performed in the maxon region. The corresponding maxon parameters Δ_M, Q_M, and μ_M (d and e are additional adjustable parameters) have been calculated by fits of ϵ_Q in the maxon region, over a wave-vector range ΔQ on the order of 0.8 Å^{-1}, to the formula

$$\epsilon_Q = \Delta_M - \frac{\hbar^2}{2m\mu_M}(Q - Q_M)^2 + d(Q - Q_M)^3 + e(Q - Q_M)^4. \quad (3)$$

The results are given in Table II.

As expected for a system approaching localization [43], the phonon and the maxon energies increase steadily with pressure, while the energy of the roton minimum decreases. The single-excitation data of Fig. 5(a) clearly show in addition a substantial flattening at the level of the maxon in the dispersion curve corresponding to a pressure of 24 bars. Earlier results at this pressure did not detect this effect [32,34], while more recent systematic results by Gibbs *et al.* [28] were limited to pressures below 20 bars. The data at 24 bars are qualitatively different from those at low pressures because the maxon energy exceeds twice the roton energy. At high pressures, the maxon excitation can therefore decay by phonon emission, exactly as in the case of higher wave vectors, at Pitaevskii's plateau [21].

We also observe the corresponding broadening of the maxon single excitation [Fig. 5(b)]: the measured maxon total width of 0.012 meV, obtained after subtraction of the instrumental resolution, is substantial compared to typical phonon and roton

TABLE II. Maxon energy Δ_M, wave vector Q_M, and effective mass μ_M; values in parentheses are one-standard-deviation errors from least-squares fits described in the text. The last column gives twice the energy of the roton gap $2\Delta_R$, for comparison with the value of Δ_M.

P (bars)	Δ_M (meV)	Q_M (Å^{-1})	μ_M	$2\Delta_R$
0	1.1966(10)	1.1073(2)	0.492(1)	1.4832(20)
5.01(2)	1.2422(10)	1.1089(3)	0.541(1)	1.4286(20)
10.01(2)	1.2668(10)	1.1150(3)	0.614(2)	1.3777(20)
24.08(2)	1.2662(10)	1.1336(4)	0.915(3)	1.2508(20)

widths (see Ref. [42] and references therein). The excitations in the maxon region broaden until they become unobservable in confined helium [17,44,45], where very high pressures can be reached before solidification.

We now concentrate on the multiexcitation region, shown in Fig. 4(a), which displays highly structured spectra for all pressures. The data for the pressures 5 and 10 bars are qualitatively similar to our previous results at saturated vapor pressure [30]. The high-resolution spectra display very clearly a threshold in energy at about 1.5 meV. This feature, which corresponds to the decay of an excitation into a pair of rotons, depends on pressure, since the roton energy depends on pressure. In addition, we observe several well-defined multiexcitation branches displaying substantial dispersion. Their gradual evolution reflects, as will be shown in Sec. VI, the change with pressure of the single-excitation dispersion.

We also observe important *qualitative* changes at high pressures. We examine first the multiexcitation region of the "ghost phonon." This multiphonon excitation, observed in our previous work, appears as a linear extension of the phonon branch [30]. We observe in the present work that the ghost-phonon intensity strongly decreases with pressure until it disappears at some pressure below 24 bars.

We also see very clearly in Fig. 1(a) a multiphonon region just above the roton branch for wave vectors of the order of 2.2–2.4 Å^{-1}. The high-resolution spectra at $E_i = 3.55$ meV only show part of this multiexcitation region, but the results have been completed by spectra taken at $E_i = 5.11$ meV at SVP and 24 bars, shown in Fig. 1. The intensity of these multiexcitations, described in detail in Sec. VI C, decreases strongly with pressure, behaving similarly to the ghost phonon.

The multiexcitation spectra are strongly modified at high pressures, as the maxon enters the multiexcitations continuum. Figure 4 shows that substantial intensity develops at this pressure for energies just above the maxon. Similar effects were also observed by Graf *et al.* [33], Talbot *et al.* [46], and Gibbs *et al.* [27–29] at a lower pressure (20 bars). The present data benefit from a sharper resolution, as can be seen by directly comparing spectra at $Q \approx 1$ Å^{-1} around the maxon peak. All these effects will be discussed in detail in Sec. VI in the context of a comparison with theoretical calculations.

V. CALCULATIONS WITH THE DYNAMIC MANY-BODY THEORY

We present in this section our calculations of the dynamic structure factor of superfluid ^{4}He at zero temperature obtained within the dynamic many-body theory [6,9].

A. State of the art of theory

Theoretical studies of the dynamic structure function in ^{4}He began with the work of Feynman [47] and Feynman and Cohen [48]. The Feynman theory of elementary excitations was developed in a systematic Brillouin-Wigner perturbation theory by Jackson and Feenberg [49–51]. An important contribution was the identification of classes of theories for the dynamic structure function [52] that satisfy the ω^0 and ω^1 sum rules exactly.

The most complete evaluation of the phonon-roton dispersion relation in terms of Brillouin-Wigner perturbation theory was carried out by Lee and Lee [53], who obtained an impressive agreement with the experimental phonon-roton spectrum up the wave vector of 2.5 Å^{-1}. The major drawback with these early calculations was that the required input, namely pair and three-body distribution functions, were poorly known.

Manousakis and Pandharipande [36,54] used input states of the Brillouin-Wigner perturbation theory including "backflow" correlations in the spirit of Feynman and Cohen. Through the gradient operator acting on the wave function, specific dynamic correlations are introduced to all orders. The "backflow function" is, however, chosen per physical intuition rather than by fundamental principles, and the evaluation of the perturbative series becomes very complicated. Topologically, diagrams similar to those of Lee and Lee [53] were included. While the accuracy of the theoretical roton energy is comparable to that of Lee and Lee, one can clearly see an inconsistency since the energy of the Pitaevskii plateau [21] lies below twice the energy of the roton gap.

The first theoretical descriptions of the multiexcitations [36,54,55] were qualitatively in agreement with the early multiexcitations data [22,32,33]. The simplest version of correlated basis functions theory produces phonon, maxon, and roton modes, as well as multiphonons. In this approximation, the calculated multiexcitations decay into Feynman modes instead of the correct single excitations; large gaps are found in the spectrum, and many predicted features are not seen in the experiments. Other features calculated in the multiexcitation region do indeed survive in recent theories, such as the presence of intensity above the phonon branch and that of a well-defined two-roton threshold (these effects are described below). These calculations, as well as many others addressing specific aspects of the multiexcitation dynamics, could not be quantitatively compared to the experimental results, but they motivated further investigations on multiparticle dynamics. Reviews can be found in Refs. [4,5].

More recent calculations [9] used a hybrid approach of Brillouin-Wigner perturbation theory and equations of motion for time-dependent multiparticle correlation functions to derive a self-consistent theory of the dynamic density-density response of ^{4}He. The self-consistency of this semianalytic method allows the identification of mode-mode coupling processes that lead to observable features in the dynamic structure function. The underlying physical mechanisms, their relationship to the ground-state structure, and the consequences on the analytic properties of the dynamic structure function emerge directly from the theory.

A very different approach involves novel numerical methods [7,8,10,15,56] that give access to dynamic properties of quantum fluids. These important algorithmic developments will reproduce, extend, and complete the experimental data with the future development of computing power; their present accuracy and consistency, however, are still limited in the multiexcitations region investigated here.

B. Dynamic many-body theory calculation

To calculate quantitatively both the single-excitation and the multiexcitation response, our calculations include up to three-body dynamic fluctuations in the correlation functions of the equations of motion [9]. We derive the self-consistent

density-density response of ^{4}He $\chi(Q,\omega)$, expressed as

$$\chi(Q,\omega) = \frac{S(Q)}{\omega - \Sigma(Q,\omega)} + \frac{S(Q)}{-\omega - \Sigma(Q,-\omega)}, \quad (4)$$

where $S(Q)$ is the static structure factor, and the self-energy $\Sigma(Q,\omega)$ is determined by the integral equation

$$\Sigma(Q,\omega) = \epsilon_0(Q) + \frac{1}{2}\int \frac{d^3p d^3k}{(2\pi)^3 n}\delta(\vec{Q}-\vec{p}-\vec{k}) \times \frac{|V^{(3)}(\vec{Q};\vec{p},\vec{k})|^2}{\omega - \Sigma(p,\omega-\epsilon_0(k)) - \Sigma(k,\omega-\epsilon_0(p))}. \quad (5)$$

In this expression, $\epsilon_0(Q)$ is the Feynman dispersion relation and $V^{(3)}$ is the three-body coupling matrix element. The simplest approximation for $V^{(3)}$, the so-called convolution approximation [51], including static ground-state triplet correlations [57], improves the density dependence of the roton minimum visibly. The most advanced calculation [6], which is taken here and in Ref. [9], sums an infinite series of diagrams, the so-called "fan diagrams," which is the minimum set of diagrams that must be included to reproduce exact features of $V^{(3)}$ for both long wavelength and short distances.

Linear-response theory [4,9] provides the relation between the experimental dynamic structure factor and the dynamic susceptibility calculated by the theory described above: the dynamic structure factor $S(Q,\omega)$ is proportional to the imaginary part of the dynamic susceptibility $\chi(Q,\omega)$, the linear response of the system to a density fluctuation.

Full maps of $S(Q,\omega)$ have been calculated for different atomic densities; see Fig. 10 in Ref. [9]. The data shown in Figs. 1 and 4 correspond to $n = 0.0215$, 0.0230, 0.0240, and 0.0255 Å^{-3}, values that provide the best overall agreement with the experiment. They turn out to be very close to the experimental results for $P = 0$, 5, 10, and 24 bars, $n_{\rm exp} =$ 0.0218, 0.0230, 0.0239, and 0.0258 Å^{-3}. The small shift in density is within the expected accuracy of the theoretical calculations.

The calculations presented here have been performed using only the most relevant diagrams [9]. This approximation is sufficient to provide an excellent description of the dynamics, but minor discrepancies can still be seen. The most salient effect is that the roton energy is overestimated; at zero pressure, for instance, the calculated value is 0.83 meV while the measured value is 0.7416(10) meV. This discrepancy could be resolved by including additional diagrams, but it does not seem necessary to perform such a tedious calculation given the quality of the agreement already achieved at this stage.

The calculation provides absolute values for the structure factor. In our previous work [30], the calculated values were multiplied by an overall normalization factor of 1.28 in order to have $Z(Q = 2$ Å$^{-1}) = 0.93$ near the roton. Here, this normalization has not been applied. Given the finite number of diagrams involved in the calculations, a factor of this order is within their estimated absolute accuracy.

C. Mode-mode coupling

Multiexcitations arise from the enhanced response of the system at particular energies and wave vectors corresponding to two or more single excitations into which they can decay. The theory considers [see Eq. (5)] the most relevant processes in which a density fluctuation $(\vec{Q},\omega)$ of wave vector $\vec{Q}$ and energy ω decays into a pair of single excitations with corresponding values $(\vec{p},\omega_p)$ and $(\vec{k},\omega_k)$. The calculations have been shown to be in excellent agreement with experiment at saturated vapor pressure [30]. Here we investigate the general pressure dependence of the dynamics, and several particularly intense mode-mode couplings. The latter were examined theoretically in Ref. [9], and additional calculations specialized to the main mode-mode couplings (phonon-phonon, phonon-roton, roton-roton, maxon-roton) can be found in Ref. [58]. The next section provides a detailed comparison between the theory and the experimental data.

VI. IDENTIFICATION OF THE MULTIEXCITATIONS

Above the sharp and intense phonon-maxon-roton dispersion curve, we observe a highly structured multiexcitation region. Multiexcitations are relatively strong if they can decay into a pair of high-intensity single-excitation modes. The energy and momentum of these pair combinations is directly related, by the conservation of energy and momentum, to those of the underlying elementary excitations. It is possible to determine the position of the main multiexcitation resonances in the dynamic structure factor map (2-phonons, 2-rotons, 2-maxons, and maxon-roton) from pure kinematic considerations, i.e., energy and momentum conservation. The challenge for microscopic theories is to predict the *intensity* of the multiexcitation spectrum, if possible in a large dynamic range. Obtaining the fine structure we observe requires a quantitative calculation of mode couplings.

We first present in this section a brief description of the kinematic constraints for different pair excitations, setting the framework for their identification. The following two subsections concentrate on new features observed in the multiexcitation spectrum, which we named "ghost phonon" and "ghost roton." We then describe a different type of multiexcitations, associated with roton-roton coupling, which we observed in particular "above the maxon" and "beyond the roton." We conclude this section with a discussion on higher-order multiexcitations, and the progressive evolution to the high-energy regime.

A. Kinematic constraints for pair excitations

The kinematic constraints calculated for the main low-energy multiexcitations are shown in Fig. 6. We use below the notation R^- and R^+ to distinguish rotons on each side of the roton minimum.

The allowed regions are necessarily located above the single-excitation dispersion curve. The P-P region is found at low wave vectors. Beyond the maxon, P-R^- excitations are allowed in a large region delimited by the dispersion curve and two lines starting at the maxon maximum and at the roton minimum, with slopes equal to $-c$ and $+c$, respectively, where c is the speed of sound. P-R^+ excitations occupy a region delimited by the dispersion curve and a line starting from the roton minimum with slope $-c$. There is a large overlap with the P-R^- region.

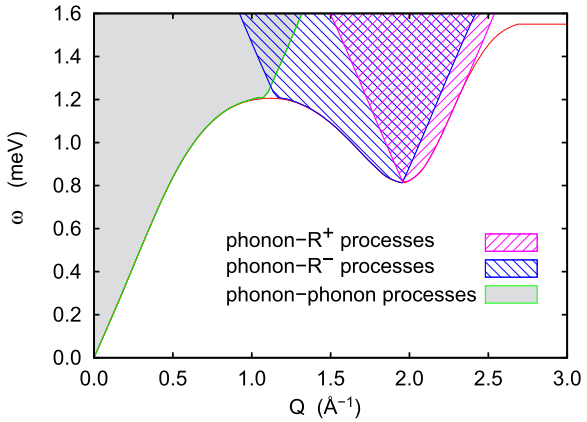

FIG. 6. Kinematically allowed regions for different multiphonon processes: P-P (including P-M^-), P-R^-, and P-R^+. See the text for details.

The case of $2R$, not shown, is particularly simple, with a threshold at twice the roton energy, $2\Delta_R$. The situation for $2M$ processes is similar, with an upper limit equal to $2\Delta_M$. M-R combinations of excitations may lead to branches with substantial dispersion. The kinematic constraints are sufficient to determine unambiguously which are the dominant processes in some multiexcitations regions, in particular at low Q above the phonon dispersion, and inside the roton parabolic dispersion curve.

The evolution of the observed multiexcitations in a large energy range, for different pressures, is illustrated in Figs. 1 and 4. We can distinguish different types of multiexcitations.

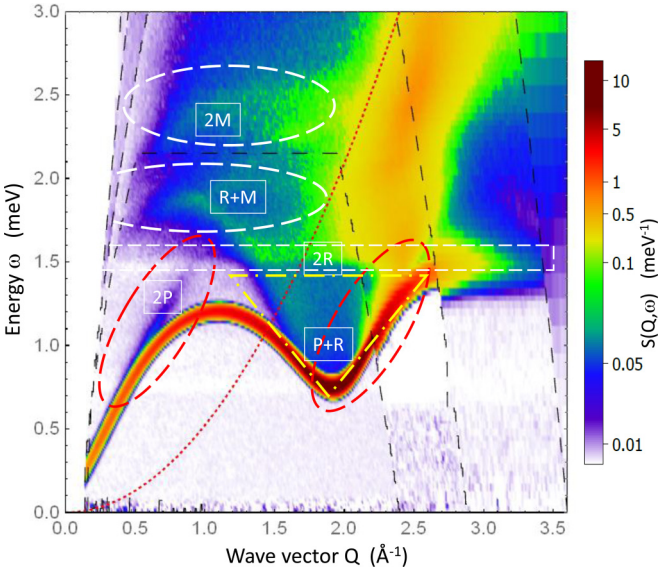

FIG. 7. Map of $S(Q,\omega)$ at SVP identifying remarkable mode-mode coupling regions: phonon-phonon ($2P$, with an ellipse around the "ghost-phonon"), phonon-roton ($P+R$, a region marked by a triangle, which includes an ellipse indicating more specifically a high-intensity "ghost-roton" region), roton-roton ($2R$, marked by a rectangle around 1.5 meV), and at higher energies the roton-maxon ($R+M$) and maxon-maxon ($2M$) regions. The description of the different lines is given in Fig. 1.

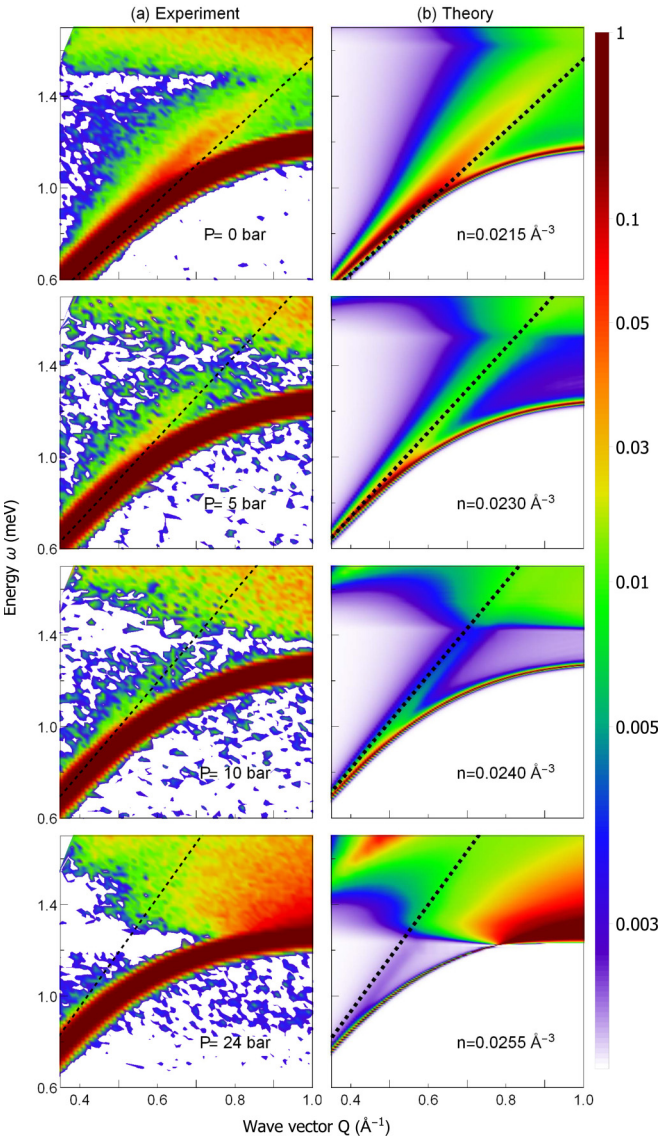

FIG. 8. Left: measured dynamic structure factor $S(Q,\omega)$ in the ghost-phonon region at $P = 0, 5, 10$, and 24 bars. The dashed straight lines correspond to the sound dispersion curve at each pressure, taken from direct measurements of the sound velocity [61]. Right: calculated dynamic structure factor at corresponding densities, $n = 0.0215$, 0.0230, 0.0240, and 0.0255 Å^{-3}, respectively (see text). The dashed straight lines correspond to the calculated sound velocities. The color-coded intensity scale is in units of meV^{-1}.

Several narrow branches are easily identified, as indicated in Fig. 7, as corresponding to $2P$, $2R$, $2M$, and M-R processes. The $2R$ feature is observed in Fig. 4 as a clear threshold, both in the theoretical and experimental data.

B. Phonon-phonon coupling: The ghost-phonon

The ghost phonon [9,30] (see Sec. IV B and Fig. 7) corresponds to a process in which a high-energy multiexcitation decays into a pair of phonons of lower energy. In the case of phonon *single excitations*, anomalous dispersion opens the phase space needed for such processes. The anomalous character of the phonon dispersion strongly decreases with

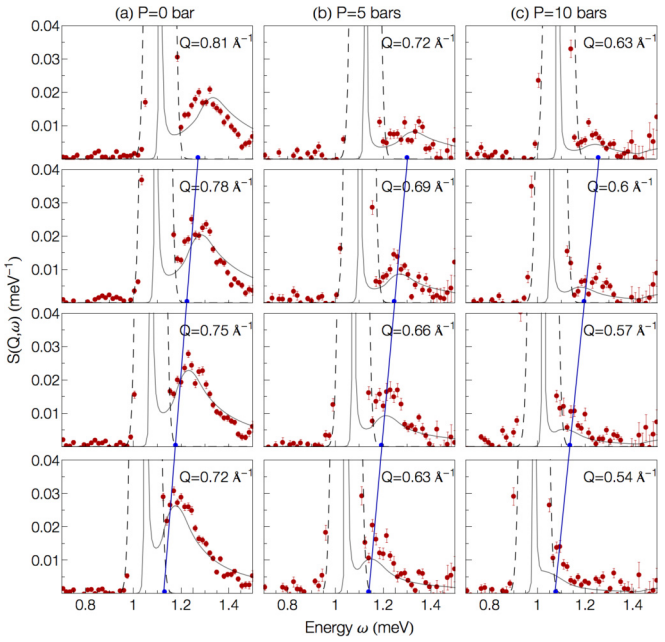

FIG. 9. Dynamic structure factor $S(Q,\omega)$ in the ghost-phonon region: spectra for different wave vectors Q at (a) $P = 0$ bar, (b) $P = 5$ bars, and (c) $P = 10$ bars. Filled circles: experimental $S(Q,\omega)$. Theoretical dynamic structure factor spectra shown as solid lines at densities $n = 0.0215$, 0.0230, and 0.0240 Å^{-3}. Dashed lines: intensity of the phonon-roton mode (cutoff) calculated directly from the self-energy [9] and convolved with the instrumental resolution of 0.07 meV. The blue lines represent the linear phonon dispersion $\epsilon_Q(P)/\hbar Q = C_0(P)$, where $C_0(P)$ is the sound velocity at a given pressure [61].

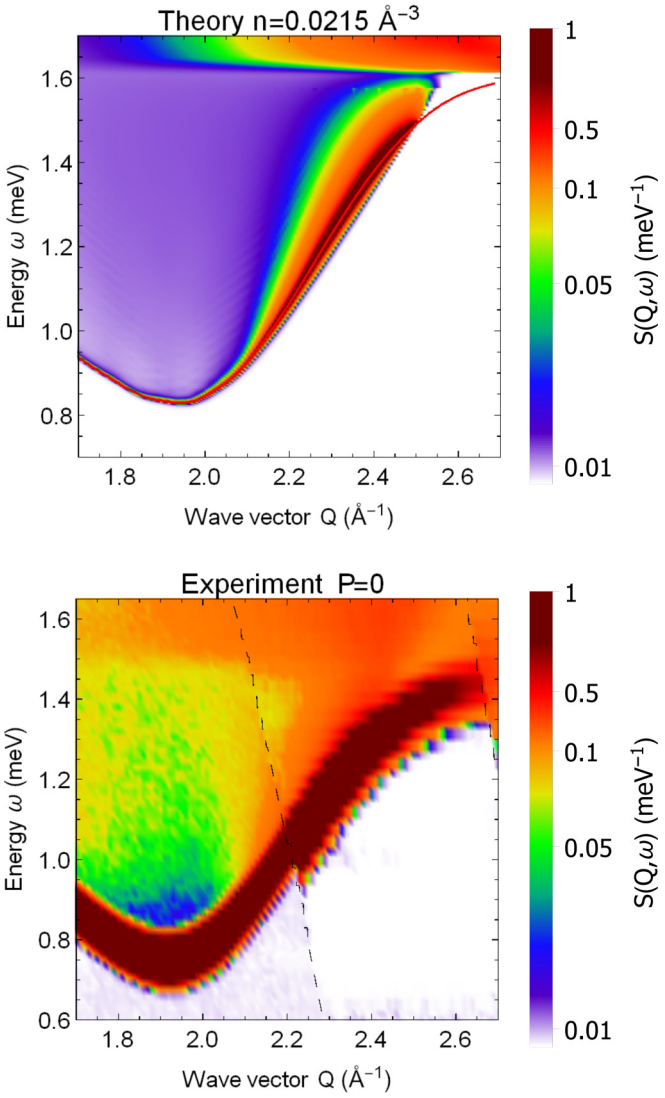

FIG. 10. Theoretical and experimental results for $S(Q,\omega)$ at saturated vapor pressure displaying enhanced multiexcitations ("ghost rotons") above the R^+ roton branch, in the supersonic rotons region. The dashed lines represent the limits of different neutron kinetic ranges; see Fig. 1. The small oscillations observed along some contours should be disregarded; they result from numerical discretization.

increasing pressure, and normal dispersion is recovered at high pressures [4,17,59,60]. The ghost-phonon intensity follows this trend: the pressure dependence is strong, and the ghost phonon is clearly suppressed at $P = 24$ bars, as shown in the experimental and theoretical results in Fig. 4, and in more detail in Fig. 8.

Cuts of $S(Q,\omega)$ at several wave vectors at the ghost-phonon level are presented for $P = 0$, 5 and 10 bars in Fig. 9. The ghost-phonon peaks for the different wave vectors are clearly located on the extension of the linear part of the phonon branch. According to the calculations (see Eq. (6.4) of Ref. [9]), the ghost phonon remains visible until twice the wave vector up to which the dispersion relation is to a good approximation linear. Indeed, Fig. 9 shows that the energy, strength, and shape of the calculated ghost phonon are in excellent quantitative agreement with the experiment at all pressures.

C. Phonon-roton coupling and the emergence of the ghost roton

One notes in Fig. 4, for all pressures, the presence of substantial intensity in the region within the roton parabola. Near the roton minimum, where P-R processes are expected to dominate, we observe that the intensity is not symmetric with respect to the roton minimum wave vector Q_R: a faint branch, clearly related to the kinematic limitation for P-R^+ processes (see Fig. 6), is seen for $Q < Q_R$, while a strong branch is formed just above the dispersion curve for $Q > Q_R$. These new features, and in particular the one for $Q > Q_R$, provide a significant contribution to the multiexcitations weight at low pressures (Fig. 10). They appear as an extension of the roton parabolic dispersion toward higher energies, and by analogy with the ghost phonon, we call these multiexcitations "ghost rotons."

It is remarkable that the intensity in this region of the P-R multiexcitations, as was the case for the ghost phonon, is high at $P = 0$, but is suppressed in the 24 bars data, as shown in Figs. 10, 11, and 12. The origin of these effects is discussed below.

Spectra for several wave vectors in the region of the ghost roton are shown in Fig. 12 at $P = 0$ and 24 bars (experiment), and in Fig. 13 for the corresponding densities $n = 0.0215$ and 0.0255 Å^{-3} (theory). We observe a good agreement between

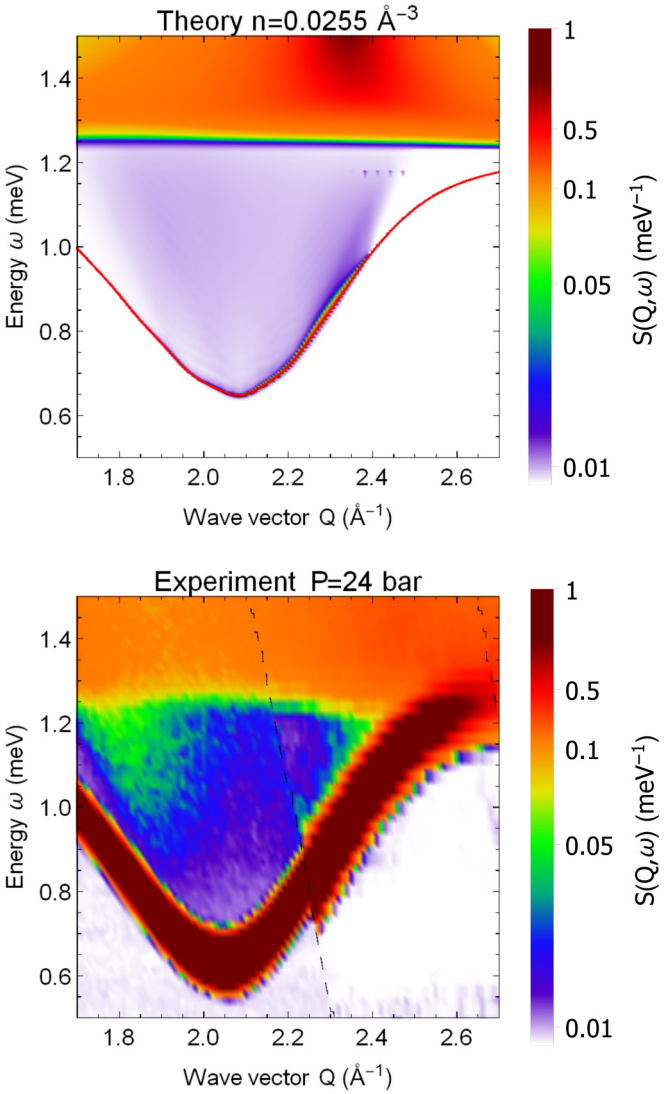

FIG. 11. Theoretical and experimental results for $S(Q,\omega)$ at $P = 24$ bars. A comparison with Fig. 10 shows that at high pressures, ghost-roton multiexcitations are strongly suppressed. They are masked by the finite-energy resolution in the experimental graph, but are still visible in the calculation.

theory and experiment, even at the highest densities, near solidification. Studies of mode-mode couplings [58,62] can therefore be most conveniently performed in the ghost phonon and the ghost-roton regions, rather than looking for a very small broadening of single excitations.

Pitaevskii [21] described the decay of *single excitations* when their group velocity reaches the velocity of sound. He named this mechanism of single-excitation broadening "type *a*." The process considered here, however, is the emission of phonons by *multiexcitations* in the vicinity of nearly supersonic single excitations. The generation of multiexcitations by neutron scattering in the R^+ rotons region by this mechanism was qualitatively predicted by Burkova [63]. Here we show that the ghost roton corresponds to this effect, that the ghost phonon is a similar effect, involving supersonic phonons, and that both are correctly predicted by the dynamic many-body theory [9].

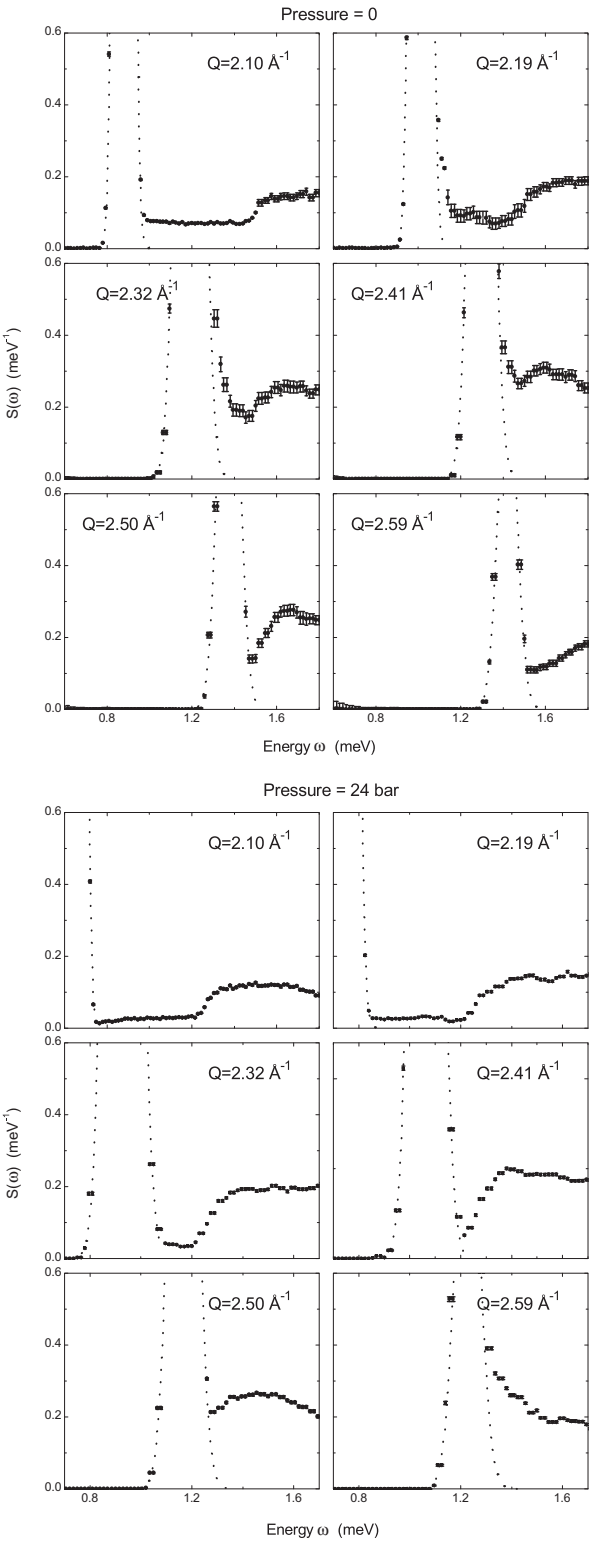

FIG. 12. $S(Q,\omega)$ measured in the region of the ghost roton at $P = 0$ (upper graph). At $P = 24$ bars (lower graph), one observes the suppression of the ghost roton. Dashed lines are Gaussian fits of the single-excitation peaks. A comparison with Figs. 10 and 11 clarifies the origin of the observed roton-peak asymmetry for some wave vectors.

It has been observed by Dietrich *et al.* [32] and confirmed by several groups (see [42] and references therein) that the

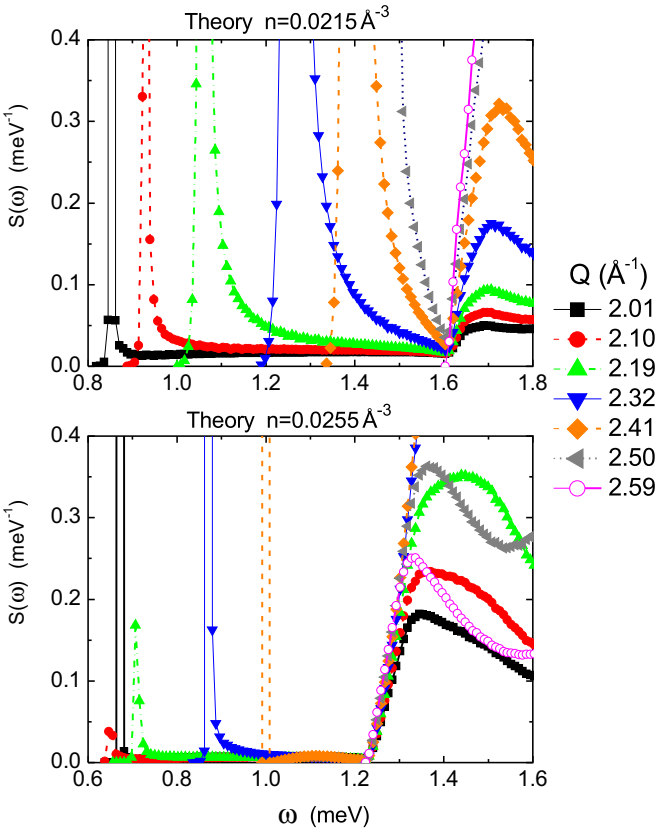

FIG. 13. $S(Q,\omega)$ calculated for wave vectors in the region of the ghost roton, at densities $n = 0.0215$ and 0.0255 Å^{-3}, associated with $P = 0$ and 24 bars, respectively.

R^+ roton group velocity reaches the sound velocity for $Q \approx 2.2$ Å^{-1} at low pressures, but it remains below the speed of sound near the melting pressure. We show in Figs. 14 and 15 our measured and calculated curves for the group velocity of the single excitations for different pressures. Two regions of interest are clearly seen: the first one, at low wave vectors, corresponds to the anomalous dispersion region and gives rise to the ghost phonon, while the second occurs for wave vectors somewhat above that of the roton minimum (and slightly below the roton minimum, but with a much smaller intensity), producing the ghost roton.

According to the analytic calculations by Burkova [63], the neutron-scattering spectrum, which corresponds to the production of one roton, should have a linear wing on the high-energy side, with a slope that depends on the wave vector. This is not really observed, either in the experimental data or in the dynamic many-body calculation: the linear part, if any, is probably not visible at the scale of the graphs (see Figs. 10, 11, 12, and 13), or is buried inside a broadened single-excitations branch.

Several effects are thus observed when the roton single excitations approach the speed of sound: a broadening of the roton branch, a downward bending of the dispersion curve, and the appearance of a multiphonon region just above the distorted dispersion curve. These effects are large at low pressures; the rapid increase of the sound velocity with pressure is responsible

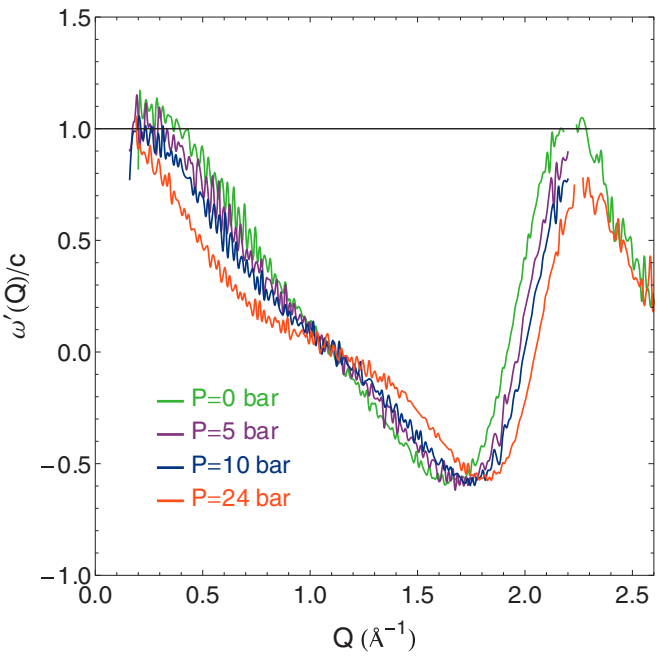

FIG. 14. The experimentally determined group velocity of single excitations normalized by the sound velocity [61], as a function of wave vector for several pressures.

for the suppression of the ghost-roton multiexcitations at 24 bars.

D. Roton-roton coupling

We discuss now a different type of *multiexcitations*, related to Pitaevskii's "type *b*" *single-excitations* decay processes in which the disintegration of a single excitation occurs as its energy exceeds twice the roton gap [21,63].

At high pressures, the maxon energy exceeds twice the roton gap, and a maxon can decay into two rotons. We described in Sec. IV B the broadening of the maxon as it enters the

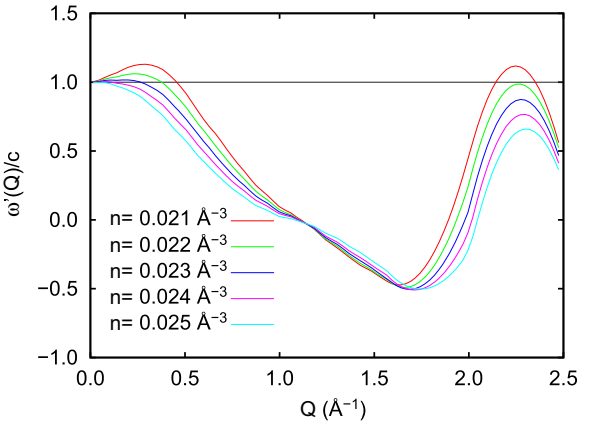

FIG. 15. The theoretically calculated group velocity of single excitations normalized by the calculated sound velocity, as a function of the wave vector, for several densities. The experimental values of the densities for $P = 0$, 5, 10, and 24 bars are $n_{\rm exp} = 0.0218$, 0.0230, 0.0239, and 0.0258 Å^{-3}.

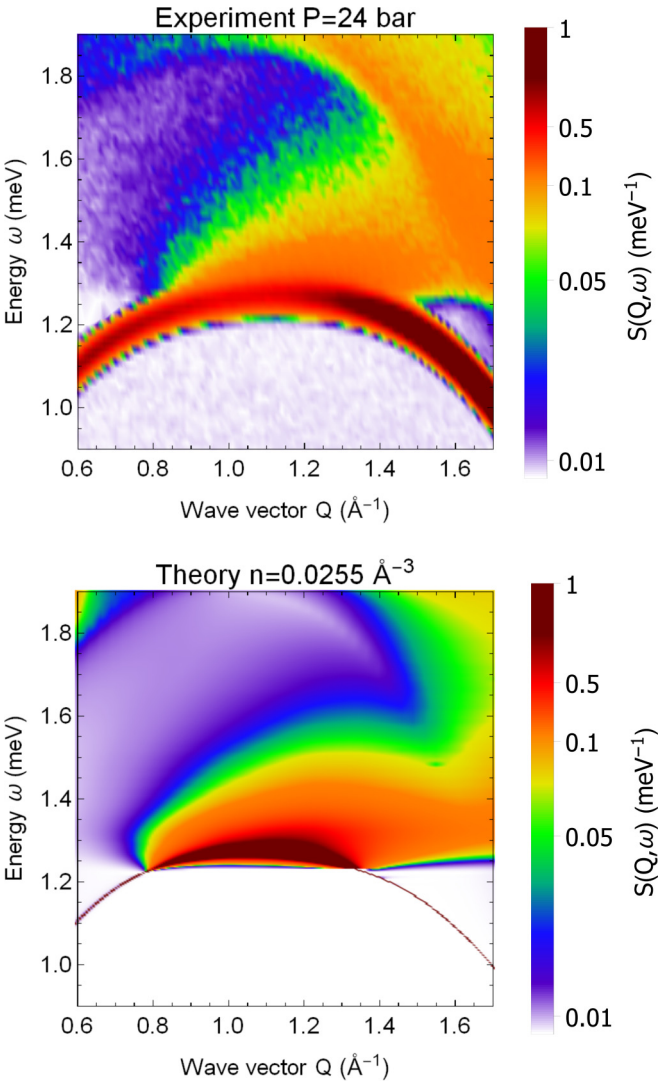

FIG. 16. $S(Q,\omega)$ in the region of the maxon at $P = 24$ bars (experiment) and at the corresponding density of 0.0255 Å^{-3} (theory).

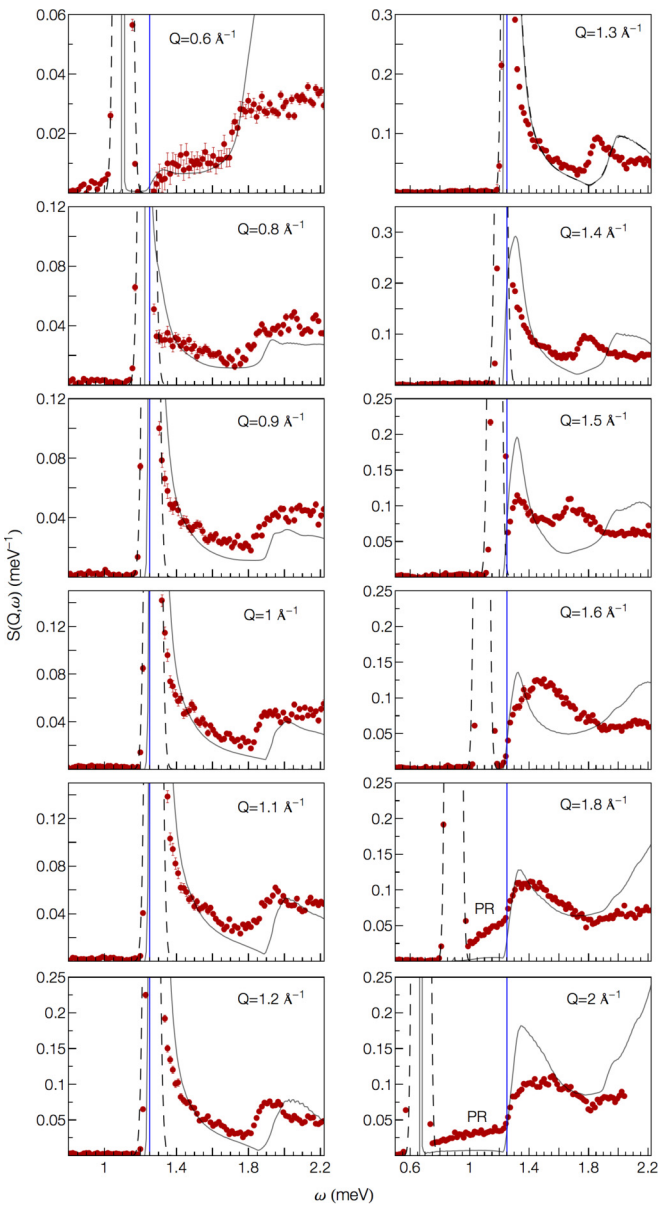

FIG. 17. Dynamic structure factor $S(Q,\omega)$: spectra for different wave vectors Q in the maxon region, at $P = 24$ bars. Filled circles: experimental $S(Q,\omega)$. Solid lines: theory at the density $n = 0.0255$ Å^{-3}. Dashed lines: intensity of the phonon-roton mode (cutoff) calculated directly from the self energy [9] and convolved with the instrumental resolution of 0.07 meV. Blue line: energy of the roton-roton threshold. PR indicates phonon-roton multiexcitations.

continuum. At 24 bars, the maxon is in the continuum of the multiexcitations for wave vectors between $Q = 0.8$ and 1.5 Å^{-1}. Under these conditions, a strong multiexcitation intensity is observed above the maxon (Figs. 16 and 17). The very characteristic "rainbowlike" measured spectrum is in very good agreement with the theoretical calculation, showing in particular that the weight of the maxon is transferred to the two-roton excitations.

The multiexcitations discussed above, observed above the maxon at high pressure, are a special case of roton-roton decay. In fact, a sharp roton-roton threshold is observed at all wave vectors (Figs. 1, 4, and 17), in regions located far from single excitations. The roton-roton threshold is, in particular, observed at low Q in the present work. It is also clear, in fact, that the intensity of the RR threshold is enhanced in the vicinity of single excitations, as was the case above the maxon at 24 bars, but also in the region above the Pitaevskii plateau. Theory and experiment display a similar shape of the spectra and intensity pattern around the roton-roton threshold, at all pressures (see Figs. 1 and 4).

E. Higher-order multiexcitations

The sharp "branches" described above correspond to decay mechanisms into two excitations. Phase-space arguments show that the signal of higher-order processes will be distributed in a rather featureless way in the energy–wave-vector space, due to the vector addition of momenta. However, the data of Fig. 1 show that the multiexcitations region at wave vectors on the order of 1.5 Å^{-1} extends to rather high energies, on the order of 4 meV. This last value constitutes a clear experimental demonstration that multiexcitations of higher order, related to

three and four single excitations (the energy of rotons and maxons is on the order of 1 meV), play a significant role in the dynamics of superfluid ^{4}He.

One can also examine the corresponding effect on the wave-vector axis, beyond the end point of the Pitaevskii plateau. The plateau could be expected to end at $2Q_R$, for a multiexcitation of energy $2\Delta_R$ decaying into two rotons of collinear wave vectors. Previous measurements [35,64,65] have found that the plateau intensity vanishes at $Q = 3.6$ Å^{-1}, considerably below $2Q_R = 3.84$ Å^{-1}. This is also observed in the present work, as seen in Figs. 1 and 3. This effect has been attributed to the decay into two rotons with an attractive R-R interaction [66], but other possible interpretations of the data are presently debated. We also note that the intensity does not extend to higher Q values at higher energies as expected for decays into three- and four-excitation processes, an effect that is probably related to the small phase-space available for collinear combinations of wave vectors. As discussed above, the energy, a scalar, is a better probe for detecting high-order multiexcitation processes. The data at 24 bars display similar effects with a simple shift toward higher wave vectors, due to the larger value of $Q_R = 2.06$ Å^{-1} at this pressure.

We now concentrate on the multiexcitation region located slightly below the free-particle dispersion curve, around 2.5 Å^{-1} (see Fig. 1). Earlier studies [22,35,67] observed a rather intense broad feature extending to higher energies. We find here a much finer structure than previously believed, and also that it depends rather strongly on the pressure. Multiexcitations in this region can only decay into three or more single excitations, which is therefore of interest for mode-mode coupling theories. The fact that we observe a high-intensity peak is probably related, at these relatively high energies, to an enhanced system response in the vicinity of the free-particle dispersion curve, which is the asymptotic behavior at higher energies. The peak at 24 bars is less intense than the corresponding one at SVP, suggesting that the maxon, strongly reduced at this pressure, is involved in the corresponding decay processes.

Finally, at the highest energies explored here, $S(Q,\omega)$ progressively converges toward the free-particle parabola, remaining below it (see Fig. 1). The so-called "glory" oscillations seen as a function of Q, both in the peak position and the width, are well documented in the literature [68]. Directly related to the corresponding oscillations in the static structure factor $S(Q)$, they result from the hard-core part of the ^{4}He-^{4}He interaction potential and from quantum coherence effects. Earlier works could not fit the spectra of the first oscillation with a single peak. The highly structured multiexcitations seen in the present work show that this peak of unusual shape results in fact from the superposition of a few multiexcitation "branches" corresponding to decays into a few single excitations. Again, the dynamic structure factor in this region depends on pressure, and the spectra for $Q \approx 3.5$ Å^{-1} are strongly affected by the collapse of the maxon.

VII. CONCLUSION

A comprehensive understanding of the dynamics of interacting Bose systems, going from the Landau quasiparticles and multiexcitation regimes up to the high-energy limit where the independent-particle dynamics is recovered, emerges from our combined experimental and theoretical work. The as yet largely unexplored multiexcitation regime has been systematically investigated. Ghost-phonon and ghost-roton regimes have been observed, associated with phonon emission in the region of nearly supersonic multiexcitations, by a Cherenkov-like process qualitatively predicted by Burkova's extension of Pitaevskii's theory. Several other multiexcitation branches or thresholds have been observed and identified in the low-energy sector, where excellent quantitative agreement is found with the predictions of the dynamic many-body theory. This agreement extends even to high pressures, near solidification, as shown, for example, for the remarkable case of the maxon disintegration into two rotons. The calculations, including specific multiparticle fluctuations to all orders [9], provide a good description of the dynamics for energies as high as 2 meV. Above this value, higher-order processes dominate the dynamics. Our high-energy/wave-vector data call for further theoretical developments in order to describe quantitatively the behavior observed at higher energies, above the simple multiexcitations region but still substantially below the quasi-free-particle (impulse-approximation) sector.

ACKNOWLEDGMENTS

We are grateful to X. Tonon for his help with the experiments. This work was supported, in part, by the Austrian Science Fund FWF Grant No. I602, the French Grant No. ANR-2010-INTB-403-01, the European Community Research Infrastructures under the FP7 Capacities Specific Programme, Microkelvin Project No. 228464, and the European Microkelvin Platform.

[1] D. Pines and P. Nozières, *The Theory of Quantum Liquids* (Addison-Wesley, Redwood City, CA, 1990).
[2] A. J. Leggett, *Quantum Liquids: Bose Condensation and Cooper Pairing in Condensed-Matter Systems* (Oxford University Press, Oxford, 2006).
[3] L. Landau, J. Phys. (Moscow) **11**, 91 (1947).
[4] H. Glyde, *Excitations in Liquid and Solid Helium*, Oxford Series on Neutron Scattering in Condensed Matter (Clarendon, Oxford, 1994).
[5] *Introduction to Modern Methods of Quantum Many-Body Theory and their Applications*, edited by A. Fabrocini, S. Fantoni, and E. Krotscheck, Advances in Quantum Many-Body Theory (World Scientific, Singapore, 2002), Vol. 7.
[6] C. E. Campbell and E. Krotscheck, Phys. Rev. B **80**, 174501 (2009).
[7] E. Vitali, M. Rossi, L. Reatto, and D. E. Galli, Phys. Rev. B **82**, 174510 (2010).
[8] A. Roggero, F. Pederiva, and G. Orlandini, Phys. Rev. B **88**, 094302 (2013).
[9] C. E. Campbell, E. Krotscheck, and T. Lichtenegger, Phys. Rev. B **91**, 184510 (2015).
[10] G. Ferré and J. Boronat, Phys. Rev. B **93**, 104510 (2016).

[11] W. Dmowski, S. Diallo, K. Lokshin, G. Ehlers, G. F. Porta, J. Boronat, and T. Egami, Nat. Commun. **8**, 15294 (2017).
[12] E. Krotscheck, J. Low Temp. Phys. **119**, 103 (2000).
[13] H. M. Böhm, R. Holler, E. Krotscheck, and M. Panholzer, Phys. Rev. B **82**, 224505 (2010).
[14] H. Godfrin, M. Meschke, H.-J. Lauter, A. Sultan, H. M. Böhm, E. Krotscheck, and M. Panholzer, Nature (London) **483**, 576 (2012).
[15] M. Nava, D. E. Galli, S. Moroni, and E. Vitali, Phys. Rev. B **87**, 144506 (2013).
[16] M. C. Gordillo and J. Boronat, Phys. Rev. Lett. **116**, 145301 (2016).
[17] H. R. Glyde, Rep. Prog. Phys. **81**, 014501 (2018).
[18] P. W. Anderson, *Concepts in Solids: Lectures on the Theory of Solids* (World Scientific, Singapore, 1997), Vol. 58.
[19] A. L. Fetter and J. D. Walecka, *Quantum Theory of Many-Particle Systems* (Dover Publications, Mineola, NY, USA, 2003).
[20] R. Donnelly, J. Donnelly, and R. Hills, J. Low Temp. Phys. **44**, 471 (1981).
[21] P. Pitaevskii, J. Exptl. Theoret. Phys. **36**, 1168 (1959) [Sov. Phys. JETP **9**, 830 (1959)].
[22] R. A. Cowley and A. D. B. Woods, Can. J. Phys. **49**, 177 (1971).
[23] E. C. Svensson, P. Martel, V. F. Sears, and A. D. B. Woods, Can. J. Phys. **54**, 2178 (1976).
[24] K. Andersen, W. Stirling, R. Scherm, A. Stunault, B. Fåk, H. Godfrin, and A. Dianoux, Physica B **180**, 851 (1992).
[25] K. Andersen, W. Stirling, R. Scherm, A. Stunault, B. Fåk, H. Godfrin, and A. Dianoux, J. Phys.: Condens. Matter **6**, 821 (1994).
[26] R. Crevecoeur, H. Smorenburg, I. deSchepper, W. Montfrooij, and E. Svensson, Czech. J. Phys. **46**, 257 (1996).
[27] M. R. Gibbs, Ph.D. thesis, Keele University, 1996.
[28] M. R. Gibbs, K. H. Andersen, W. G. Stirling, and H. Schober, J. Phys.: Condens. Matter **11**, 603 (1999).
[29] M. R. Gibbs, W. G. Stirling, K. H. Andersen, and H. Schober, J. Low Temp. Phys. **120**, 55 (2000).
[30] K. Beauvois, C. E. Campbell, J. Dawidowski, B. Fåk, H. Godfrin, E. Krotscheck, H.-J. Lauter, T. Lichtenegger, J. Ollivier, and A. Sultan, Phys. Rev. B **94**, 024504 (2016).
[31] T. R. Prisk, M. S. Bryan, P. E. Sokol, G. E. Granroth, S. Moroni, and M. Boninsegni, J. Low Temp. Phys. **189**, 158 (2017).
[32] O. W. Dietrich, E. H. Graf, C. H. Huang, and L. Passell, Phys. Rev. A **5**, 1377 (1972).
[33] E. H. Graf, V. J. Minkiewicz, H. B. Møller, and L. Passell, Phys. Rev. A **10**, 1748 (1974).
[34] W. G. Stirling, in *Excitations in Two-Dimensional and Three-Dimensional Quantum Fluids*, edited by A. F. G. Wyatt and H. J. Lauter (Springer, Boston, 1991), pp. 25–46.
[35] J. V. Pearce, R. T. Azuah, B. Fåk, A. R. Sakhel, H. R. Glyde, and W. G. Stirling, J. Phys.: Condens. Matter **13**, 4421 (2001).
[36] E. Manousakis and V. R. Pandharipande, Phys. Rev. B **30**, 5062 (1984).
[37] LAMP, http://www.ill.fr/data_treat/lamp/lamp.html.
[38] J. Dawidowski, F. J. Bermejo, and J. R. Granada, Phys. Rev. B **58**, 706 (1998).
[39] J. Dawidowski, J. Santisteban, and J. Granada, Physica B **271**, 212 (1999).
[40] V. F. Sears, Adv. Phys. **24**, 1 (1975).
[41] A. Woods, P. Hilton, R. Scherm, and W. Stirling, J. Phys. C **10**, L45 (1977).
[42] T. Keller, K. Habicht, R. Golub, and F. Mezei, Europhys. Lett. **67**, 773 (2004).
[43] P. Nozières, J. Low Temp. Phys. **137**, 45 (2004).
[44] J. V. Pearce, J. Bossy, H. Schober, H. R. Glyde, D. R. Daughton, and N. Mulders, Phys. Rev. Lett. **93**, 145303 (2004).
[45] J. Bossy, J. V. Pearce, H. Schober, and H. R. Glyde, Phys. Rev. Lett. **101**, 025301 (2008).
[46] E. F. Talbot, H. R. Glyde, W. G. Stirling, and E. C. Svensson, Phys. Rev. B **38**, 11229 (1988).
[47] R. P. Feynman, Phys. Rev. **94**, 262 (1954).
[48] R. P. Feynman and M. Cohen, Phys. Rev. **102**, 1189 (1956).
[49] H. W. Jackson and E. Feenberg, Rev. Mod. Phys. **34**, 686 (1962).
[50] H. W. Jackson, Phys. Rev. **185**, 186 (1969).
[51] H. W. Jackson, Phys. Rev. A **8**, 1529 (1973).
[52] H. W. Jackson, Phys. Rev. A **9**, 964 (1974).
[53] D. K. Lee and F. J. Lee, Phys. Rev. B **11**, 4318 (1975).
[54] E. Manousakis and V. R. Pandharipande, Phys. Rev. B **33**, 150 (1986).
[55] W. Götze and M. Lücke, Phys. Rev. B **13**, 3825 (1976).
[56] M. Boninsegni and D. M. Ceperley, J. Low Temp. Phys. **104**, 339 (1996).
[57] C. C. Chang and C. E. Campbell, Phys. Rev. B **13**, 3779 (1976).
[58] See Supplemental Material at http://link.aps.org/supplemental/10.1103/PhysRevB.91.184510 on mode-mode couplings.
[59] H. J. Maris and W. E. Massey, Phys. Rev. Lett. **25**, 220 (1970).
[60] H. J. Maris, Rev. Mod. Phys. **49**, 341 (1977).
[61] B. M. Abraham, Y. Eckstein, J. B. Ketterson, M. Kuchnir, and P. R. Roach, Phys. Rev. A **1**, 250 (1970).
[62] B. Fåk, T. Keller, M. E. Zhitomirsky, and A. L. Chernyshev, Phys. Rev. Lett. **109**, 155305 (2012).
[63] A. Burkova, J. Exptl. Theoret. Phys. **81**, 600 (1981) [Sov. Phys. JETP **54**, 320 (1981)].
[64] B. Fåk and J. Bossy, J. Low Temp. Phys. **112**, 1 (1998).
[65] H. R. Glyde, M. R. Gibbs, W. G. Stirling, and M. A. Adams, Europhys. Lett. **43**, 422 (1998).
[66] F. Pistolesi, Phys. Rev. Lett. **81**, 397 (1998).
[67] B. Fåk and K. Andersen, Phys. Lett. A **160**, 468 (1991).
[68] K. H. Andersen, W. G. Stirling, and H. R. Glyde, Phys. Rev. B **56**, 8978 (1997), and references therein.